Superradiance Coherence Sizes in Single-Molecule Spectroscopy of LH2 Antenna Complexes

Yang Zhao,[†] Torsten Meier,[§] Wei Min Zhang,[†,‡] Vladimir Chernyak,[‡] and Shaul Mukamel*[,†,‡]

Rochester Theory Center for Optical Science and Engineering and Department of Chemistry, University of Rochester, Rochester, New York 14627, and Department of Physics and Material Sciences Center, Philipps University, Renthof 5, D-35032 Marburg, Germany

Received: January 11, 1999; In Final Form: March 16, 1999

The distribution of cooperative radiative decay rates in photosynthetic aggregates is calculated using a Frenkel exciton model with static diagonal disorder. This distribution which depends on both the exciton coherence sizes and the aggregate geometry can be directly observed using single-molecule spectroscopy. Comparison is made with a dynamic exciton self-trapping (polaron) mechanism for localization.

I. Introduction

Recent X-ray diffraction measurements have determined the 2.5 Å resolution structure of the LH2 antenna complex of purple bacteria.[1] The antenna is made of an inner ring (the B850 system) with 18 bacteriochlorophyll *a* (BCl*a*) molecules and an outer ring (the B800 system) with 9 BCl*a*. Cyclic complexes appear also in other systems such as LH1 which has 32 chlorophylls. Optical properties of these photosynthetic antenna complexes have been studied by various time- and frequency-resolved measurements including fluorescence depolarization,[2,3] hole burning,[4−8] pump-probe,[9−12] and photon echoes.[13,14]

One of the objectives of the study of photosynthetic antenna complexes is to find out whether the elementary optical excitations are localized on a few molecules or delocalized on the entire complex. The coherence size of the excitations is determined by the interplay of intermolecular couplings and (static as well as dynamic) disorder. It has been shown that the system is characterized by a multitude of coherence sizes associated with various dynamical variables. The splitting of the positive (induced absorption) and negative (bleaching) peaks in pump-probe spectroscopy is related to the exciton mean free path.[15] Cooperative spontaneous emission (superradiance) is, on the other hand, controlled by a different coherence size associated with the exciton density matrix[16]

$$\rho_{mn} \equiv \langle B_m^\dagger B_n \rangle \tag{1.1}$$

where B_n ($B_n^\dagger$) are exciton annihilation (creation) operators for the nth molecule, and the expectation value is over all electronic and nuclear coordinates. The radiative decay rate of an aggregate (Γ_S) measured in units of the radiative rate of a single chromophore is known as the superradiant coherent factor. It is related to the exciton density matrix ρ_{mn} by[15,16]

$$\Gamma_S = \sum_{mn} \rho_{mn} \mathbf{d}_m \cdot \mathbf{d}_n \tag{1.2}$$

where $\mathbf{d}_m$ is a unit vector in the direction of the mth chromophore transition dipole. Γ_S depends on the exciton coherence size through ρ_{mn} as well as on the geometry (relative orientation of transition dipoles) through the $\mathbf{d}_m \cdot \mathbf{d}_n$ factors.

Excitonic and polaritonic superradiance also shows up in semiconductor quantum wells,[17−20] quantum wires,[21] and σ-conjugated polysilanes.[22,23] The localization mechanisms include static disorder, exciton−phonon coupling, and impurity trapping. In a previous paper,[16] we examined the effects of exciton−phonon coupling and static disorder on excitonic coherence and superradiance of the B850 system in LH2. Measurements of the temperature-dependent radiative lifetime in LH2[24] can be interpreted using a diagonal disorder model.[15] In our previous work we have explored the temperature dependences of the radiative rate averaged over realizations of disorder.[16] The time-resolved fluorescence signal

$$S(\tau) = \gamma \exp(-\Gamma_{\mathrm{nr}}\tau) \int \mathrm{d}\Gamma_S P(\Gamma_S) \Gamma_S \exp(-\gamma \Gamma_S \tau) \tag{1.3}$$

contains detailed information on the distribution $P(\Gamma_S)$ itself through its Laplace transform rather than its average or peak values. Here γ is the single chromophore radiative rate, and Γ_{nr} is the nonradiative decay rate which is assumed to be independent on disorder. The signal can be expressed in terms of the average rate only if the distribution is sharply peaked around its average value.

Among the most recent additions to the arsenal of techniques applied to the antenna complexes is the utilization of single-molecule spectroscopy (SMS) which can provide a direct probe for $P(\Gamma_S)$.[25] Studies of single molecules in condensed phase is an exciting new development combining[26−32] various forms of optical microscopy with ultrasensitive detection SMS at low temperatures which requires selecting a photostable molecule with a narrow zero-phonon line and high fluorescence yield, using a narrow band laser and focusing on only a tiny volume of the sample. This allows a much closer comparison between experiment and microscopic theories of the host dynamics. Unlike scanning tunneling microscopy (STM) and atomic force microscopy (AFM) which probe atoms and molecules well-bonded on surfaces, SMS operates noninvasively in the optical far field with a spatial resolution of the order of the optical wavelength and can be used to study single molecules hidden deep within a solid matrix. Direct visualization of processes involving single molecules in condensed phase at low temper-

[†] Rochester Theory Center for Optical Science and Engineering.
[‡] Department of Chemistry, University of Rochester.
[§] Philipps University.

10.1021/jp990140z CCC: $18.00
Published on Web 04/22/1999

ature is now made possible with the incorporation of time-resolved techniques.[32−37] SMS distributions of fluorescence lifetimes and photobleaching properties of single LH2 complexes have also been measured under physiological conditions.[25] Low-temperature (1.2 K) single-molecule fluorescence excitation spectra of these complexes have been reported as well.[38] The photobleaching of one Bchl molecule causes the complete shutdown of fluorescence due to exciton trapping. Bulk measurements on LH2[24] reveal that $\Gamma_S \sim 2-3$ and is virtually independent on temperature between 4 and 200 K. SMS measurements of LH2 complexes should provide the entire distribution of radiative times.

In this paper we compute the distribution of radiative lifetimes resulting from a static disorder mechanism for exciton localization. For comparison we also present the corresponding distribution induced by strong coupling to phonons and polaron formation. The resulting distributions show distinct signatures of both models. Effects of static disorder on radiative rate distributions of thermally equilibrated rapidly relaxing excitons are calculated in section II. The distributions for slowly relaxing excitons are presented in section III. The corresponding distributions for strong exciton−phonon coupling resulting in the formation of polarons are calculated in section IV. Our results are finally discussed in section V.

II. Radiative Rate Distributions for Rapidly Relaxing Excitons with Static Diagonal Disorder

We model the B850 band of the LH2 antenna complex of purple, bacteria as a one-dimensional circular aggregate made out of two-level molecules with a Frenkel exciton Hamiltonian written using creation (annihilation) operators $B_m^\dagger$ (B_m)[39]:

$$\hat{H} = \sum_n \Omega_n B_n^\dagger B_n + \sum_{mn}^{m\neq n} J_{mn} B_m^\dagger B_n \qquad (2.1)$$

The coupling $J_{n,n+1}$ between adjacent BCl*a* molecules in the B850 band alternates between the value 273 and 291cm^{-1}. We shall neglect this (weak variation and use an average coupling) parameter J. In the absence of disorder, the one-exciton eigenstates Ψ_α and energies ϵ_α are given by

$$\Psi_\alpha(m) = \frac{1}{\sqrt{N}} e^{iK_\alpha m};\ \epsilon_\alpha = 2J\cos(K_\alpha) \qquad (2.2)$$

with crystal momenta $K_\alpha = 2\pi\alpha/N$, $\alpha = -N/2+1, -N/2+2, ..., -1, 0, 1, ..., N/2$ ($N = 18$ is the number of chromophores). The transition dipoles are known to be oriented almost in the plane in the head-to-head and tail-to-tail configurations, and the nearest-neighbor intermolecular coupling is positive. Following refs 15 and 16, we apply a transformation $B_n \rightarrow (-1)^n B_n$ of the exciton operators which results in tangential orientations of the transition dipoles and a negative intermolecular coupling $J = -280$ cm^{-1} which is reminiscent of J aggregates.[40] For comparison we also consider a system with the same negative J and vertical dipole orientations (Figure 1).

In this section we assume that relaxation among exciton states is fast compared with their radiative decay rates. The reduced density matrix is therefore thermally equilibrated at all times during the spontaneous emission process and assumes the form

$$\rho_{mn} = Z^{-1} \sum_\alpha \Psi^*{}_\alpha(m)\Psi_\alpha(n) \exp(-\epsilon_\alpha/k_B T) \qquad (2.3)$$

where $Z \equiv \sum_\alpha \exp(-\epsilon_\alpha/k_B T)$, T is the temperature, and

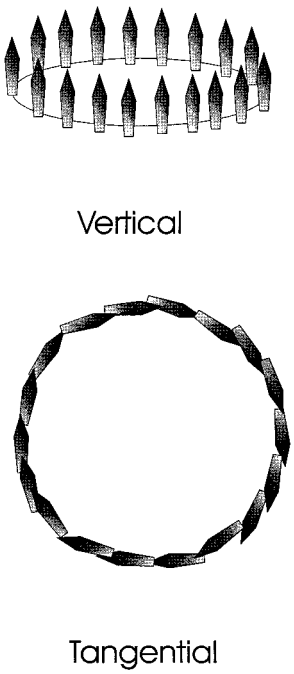

Figure 1. Two dipole configurations for cyclic aggregates used in this article. LH2 has the tangential geometry; the vertical geometry is given for comparison.

$\Psi_\alpha(n)$ is the normalized wavefunction for the α'th exciton. Substituting eq 2.3 into eq 1.2 we can express the radiative rate using the exciton basis set

$$\Gamma_S = Z^{-1} \sum_\alpha f_\alpha \exp(-\epsilon_\alpha/k_B T) \qquad (2.4)$$

where the radiative rate of the α'th exciton γf_α is determined by it's oscillator strength,

$$f_\alpha = \sum_{mn} \mathbf{d}_m \cdot \mathbf{d}_n \Psi_\alpha{}^*(m)\Psi_\alpha(n) \qquad (2.5)$$

The total oscillator strength of the aggregate $\sum_\alpha f_\alpha = N$ is concentrated in no more than three superradiant states which are not necessarily eigenstates of the one-exciton Hamiltonian.[16] However, in the absence of disorder, by symmetry, the superradiant states are also one-exciton eigenstates. For the vertical configuration there is a single superradiant state with $f = N$ which is the lowest-energy ($\alpha = 0$) state. For the tangential configuration the oscillator strength is shared by two exciton states with $\alpha = \pm 1$ and $f = N/2$. This implies that the maximum possible radiative rate for the vertical (tangential) configuration is $\Gamma_S = N = 18$ ($\Gamma_S = N/2 = 9$). Disorder breaks the translational symmetry so that the superradiant states are no longer eigenstates of the single-exciton Hamiltonian and the oscillator strength is distributed among all exciton states. We adopt a diagonal disorder model, i.e.; the chromophore transition frequencies are given by $\Omega_n = \Omega + \xi_n$. ξ_n have a Gaussian uncorrelated distribution with zero mean and fwhm σ. For each value of σ, the distribution of radiative rates was computed using eqs 2.4 and 2.5, by summing over 100 000 disorder realizations. We have performed the simulations for two values of disorder: weak disorder $\sigma = 190$ cm^{-1}, and strong disorder $\sigma = 950$ cm^{-1}. The reason for this particular choice will be explained in the Discussion section.

The calculated distribution of radiative rates $P(\Gamma_S)$ for weak disorder and vertical geometry is shown in Figure 2a. At $T = 1$ K the distribution is broad and has a maximum at about

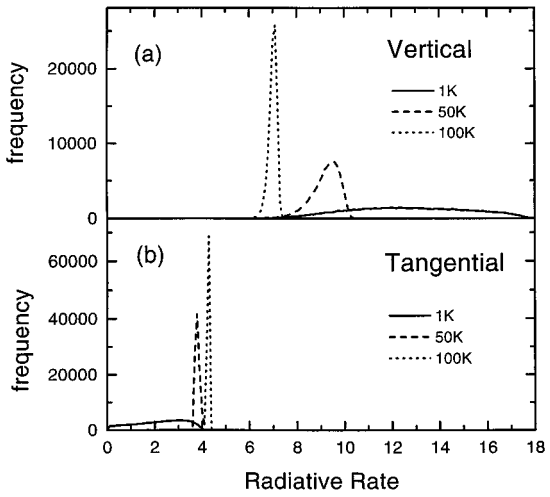

Figure 2. Distribution of radiative rates Γ_S (in units of the single-molecule rate) for weak static diagonal disorder with $\sigma = 190$ cm^{-1} and various temperatures (as indicated in each panel). Calculations involved averaging over 100 000 realizations of disorder. A bin size of 0.1 is used for the radiative rate to create the histogram: (a) vertical dipole configuration; (b) tangential dipole configuration.

12, which reflects the coherence size L_ρ related the off-diagonal size of the exciton density matrix.[16] At this temperature, only the lowest exciton state is populated for each realization; thus the distribution directly reflects the disorder-induced localization length of the lowest exciton. L_ρ is related to the exciton localization length l_A by[16] $L_\rho \approx 3l_A$. For the vertical dipole configuration, the radiative rate $\Gamma_S \approx L_\rho$ which implies that the distribution of the lowest-energy exciton states peaks at $l_A \approx 4$. At higher temperatures, higher exciton states are populated and contribute to the superradiance (cf. eq 1.2). Figure 2a shows that the maximum of the distribution is at $\Gamma_S^* = 9.5$ for $T = 50$ K and $\Gamma_S^* = 7$ for $T = 100$ K. The decrease of Γ_S^* with increasing temperature makes sense since the higher energy states populated at higher temperatures are oscillatory and, therefore, carry a lower oscillator strength.

A less obvious observation is that the distribution narrows as the temperature is increased. This can be explained by making use of a correlation between the localization length l_A of the lowest exciton state and the energy gap ϵ between the lowest two exciton states. Using the optimal fluctuation approach[41] it can be shown that the lower the energy gap ϵ, the smaller is the localization length l_A. Since the lowest exciton carries most of the oscillator strength (typical value is $f_0 = 12$) the radiative rate is given by $\Gamma_S \approx P_0 f_0$, where $P_\alpha = Z^{-1} \exp(-\epsilon_\alpha/k_B T)$ denotes the thermal distribution factor in eq 2.3. Suppose we have a realization (1) of disorder which gives a certain value of Γ_S at some finite temperature T. A different realization (2) which corresponds to a higher value of ϵ will imply a lower, value of the localization length l_A and a reduced f_0: $f_0^{(2)} < f_0^{(1)}$. However, the increase of ϵ leads to the increase of the lowest exciton population factor P_0: $P_0^{(2)} < P_0^{(1)}$. This implies that the fluctuations of $\Gamma_S \approx P_0 f_0$ are smaller than those of f_0. This compensation mechanism, with its increasing role at higher temperatures, leads to a partial cancellation of fluctuations in the distribution of Γ_S and narrows the distribution at higher temperatures. In the infinite-temperature limit, all single excitons are populated equally for a single realization of disorder, all superradiant effects are lost, and L_ρ and Γ_S are both equal to 1.

We now turn to the tangential geometry (Figure 2b). In the absence of disorder the lowest $\alpha = 0$ exciton state is dark, and the following two $\alpha = \pm 1$ degenerate states each carry an oscillator strength of 9. Only the lowest exciton state contributes at $T = 1$ K. In the absence of disorder we get $L_\rho = 18$ and $\Gamma_S = 0$, since for the tangential dipole orientation the vector sum of the dipoles is zero. For weak disorder the distribution of L_ρ is peaked around $L_\rho = 12$. This implies that the nonzero value of Γ_S is due to the partial loss of coherence which yields a distribution of Γ_S between $\Gamma_S = 0$ and $\Gamma_S = 4$ peaked at $\Gamma_S \approx 3$.

Many properties of the distributions of Γ_S can be understood using the following representation for the distribution:[42]

$$P(\Gamma_S) = \int_{\Omega(\Gamma_S,T)} \mathbf{d}\boldsymbol{\xi} \exp[-W(\boldsymbol{\xi})] \tag{2.6}$$

where $\Omega(\Gamma_S,T)$ denotes the subspace of the diagonal disorder realization parameters $\boldsymbol{\xi} = (\xi_1, ..., \xi_N)$ which yield the radiative rate Γ_S at temperature T. dξ stands for the proper measure of integration defined in ref 42, and $W(\boldsymbol{\xi})$ represents the distribution of diagonal disorder. For the present Gaussian disorder model it adopts the form

$$W(\boldsymbol{\xi}) = \frac{1}{2\sigma^2}\sum_{j=1}^{N} \xi_j^2 \tag{2.7}$$

At $T = 0$ the minimal value of $\Gamma_S = 0$ is achieved, e.g., at $\xi = 0$ with the statistical weight $\exp[-W(\boldsymbol{\xi})] = 1$. The distribution function $f(\Gamma_S)$ vanishes for $\Gamma_S \rightarrow 0$ due to the decrease of the phase-space volume

$$v(\Omega) \equiv \int_\Omega \mathrm{d}\boldsymbol{\xi} \tag{2.8}$$

We note that $v(\Omega) \rightarrow 0$ at $\Gamma_S \rightarrow 0$ for $T = 0$ since at $\Gamma_S = 0$, $\Omega(\Gamma_S)$ becomes a manifold of a lower $(N - 2)$ dimensionality. The maximal value at $T = 0$ is $\Gamma_S^{(m)} = N/4 = 4.5$. The lowest exciton wave functions which correspond to $\Gamma_S^{(m)}$ can be parametrized as follows[42]

$$\Psi(m) = \frac{2}{N}\cos\left(\frac{2\pi m}{N} + \theta\right) \tag{2.9}$$

for all m for which the rhs of eq 2.9 is positive, and $\Psi(m) = 0$ for those m that correspond to the negative values of the rhs of eq 2.9. For any value of θ this wavefunction yields $\Gamma_S = N/4$. Since the lowest exciton wave function does not change sign, the maximal value $\Gamma_S^{(m)}$ may not be attained for any realization of disorder, as opposed to the lowest value $\Gamma_S = 0$ and $\Gamma_S = \Gamma_S^{(m)}$ which constitutes an accumulation point.[42] $P(\Gamma_S)$ vanishes at $\Gamma_S^{(m)}$ due to different reasons compared to its vanishing at $\Gamma_S = 0$: $W(\xi) \rightarrow \infty$ when ξ belongs to $\Omega(\Gamma_S)$, whereas $\Gamma_S \rightarrow \Gamma_S^{(m)}$, and therefore, the statistical weight $\exp[-W(\xi)]$ vanishes rapidly.

At higher temperatures, the distributions presented in Figure 2b are much narrower and their maxima shift toward larger values of Γ_S. This can be rationalized as follows: the low-temperature distribution shows a typical value $f_0 \approx 3$ for the oscillator strength of the lowest exciton. As will be demonstrated later, the remaining oscillator strength is almost uniformly distributed among two higher-energy excitons with a typical value $f_1 \approx f_2 \approx 7.5$. This yields $\Gamma_S \approx P_0 f_0 + 2P_1 f_1$ (for simplicity we set $P_2 \approx P_1$ and $f_2 \approx f_1$ in our estimates). Increasing the temperature leads to higher populations of excitons which carry most of the oscillator strength. This results in the increase of Γ_S and, therefore, in the shift of the maximum positions. Narrow distributions at higher temperatures originate from the compensating mechanism, similar to the vertical dipole configuration. In the tangential case, the mechanism works in a different

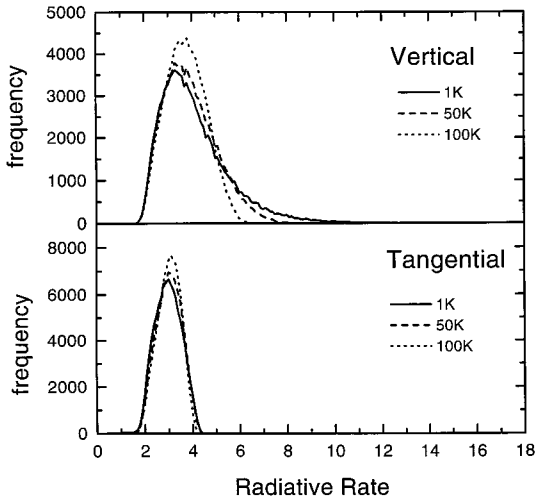

Figure 3. Same as in Figure 2 but for strong static diagonal disorder with $\sigma = 950$ cm^{-1}.

way. For two realizations of disorder $\epsilon^{(2)} > \epsilon^{(1)}$ we have $l_A^{(2)} < l_A^{(1)}$. However, in contrast to the vertical dipole orientation, we have for the lowest exciton oscillator strength $f_0^{(2)} > f_0^{(1)}$. This is the case because, as shown earlier, for these values of disorder a typical localization length is lA ≈ 4 which corresponds to a density-matrix coherence size of $L_\rho \approx 12$. In this situation the nonzero dipole is due to the loss of coherence. Therefore as l_A is decreased there is further loss of coherence and f_0 increases which increases Γ_S. The compensating mechanism works in the following way. Since $\epsilon^{(2)} > \epsilon^{(l)}$ the higher states for the second realization of disorder are less populated compared to the first realization $P_1^{(2)} < P_1^{(1)}$. However, in the present case the higher states carry most of the oscillator strength $f_1 > f_0$, and decreasing their population decreases Γ_S. Thus increase of Γ_S due to increasing f_0 is compensated by the decrease of Γ_S due to the redistribution of exciton populations.

We next turn to the strong disorder $\sigma = 950$ cm^{-1} case. The distributions of Γ_S for vertical and tangential configurations are presented in Figure 3. All distributions now show an extremely weak temperature dependence between $T = 0$ and 100 K. This means that the typical gap ϵ between the lowest and the higher states substantially exceeds the temperature $T = 100$ K, and all distributions basically reflect the distribution of the lowest exciton oscillator strength. The compensating mechanism which partially cancels the fluctuations for weaker disorder does not apply for strong disorder. This is why the distributions of Γ_S at $T = 50$ and 100 K for weak disorder are much narrower compared to their strong disorder counterparts. The distributions of Γ_S peak at the same value of $\Gamma_S^* = 3$ for both geometries as opposed to the weak disorder case. This means that $L_\rho \approx 3$; i.e., the number of chromophores emitting coherently is about 3. Since for the tangential configuration three adjacent chromophores have almost parallel dipoles, the distributions for both configurations are similar. The longer tail at larger Γ_S for the vertical configuration can be rationalized as follows. For larger values of L_ρ the dipoles for the tangential orientation are no longer parallel, which reduces Γ_S and therefore decreases the probability of realizations with high values of Γ_S.

We have shown earlier[16,15] that the same value of Γ_S averaged over disorder can be obtained using two values of disorder: either strong disorder where $L_\rho \ll N$ and $\Gamma_S \approx L_\rho$ or weak disorder where $N - L_\rho \ll N$ and $\Gamma_S \approx N - L_\rho$. Our calculations demonstrate that the distribution of Γ_S in the former case is much broader. One can, therefore, distinguish between the two situations by inspecting the distributions of Γ_S. This can be done experimentally either using SMS or by observing the time-resolved fluorescence profile: weak disorder should give an exponential decay, as opposed to the multiexponential decay predicted for strong disorder, reflecting the broad distribution of decay rates.

III. Radiative Rate Distribution of Slowly Relaxing Excitons

The calculations of section II assume a fast relaxation of exciton populations so that the exciton density matrix is thermalized during the radiative decay process. In the opposite limit of slow relaxation, each aggregate remains in one of the exciton eigenstates during a measurement and SMS will reflect the distribution of exciton oscillator strengths f_α. The relative contribution of various excitons will depend on the details of the excitation process (e.g., pump field frequency, envelope, and duration). In this section we assume thermally weighted contribution for individual exciton rates computed in the following way: for a given realization of disorder, we get N values f_0, ..., f_{N-1} which correspond to all N excitons. The αth exciton contribution is then counted with the thermal weight factor P_α, and an ensemble average over disorder is performed. The resulting $P(f_\alpha)$ distributions do not correspond to any specific measurement (since in the slow relaxation limit the thermal distribution does not apply). However, they provide an insight into the microscopic origin of the distributions and support the arguments presented above for the shapes of the distribution $P(\Gamma_S)$ of radiative rates at different temperatures.

The distributions $P(f_\alpha)$ for the vertical dipole configuration are presented in Figure 4a. At $T = 1$ K (upper panel) we recover the distribution of Γ_S at the same temperature shown in Figure 2a. This is to be expected since at this temperature both distributions reflect basically that of the lowest exciton oscillator strength f_0. At higher temperatures (middle and lower panels), the distributions show an additional peak close to zero originating from the oscillatory states populated at higher temperatures which have low oscillator strengths. This supports the compensating mechanism introduced earlier: increase of ϵ populates the lowest exciton which increases Γ_S, whereas the depopulation of the higher states only weakly affects Γ_S since these states are almost dark.

The computed distributions for the tangential configuration are presented in Figure 4b. The low-temperature distribution shown in the upper panel, as well as in the vertical orientation case, coincides with the distribution of Γ_S (Figure 2b) for the same reason. The distribution for $T = 50$ K (middle panel) shows an additional peak at $f = 8$. The maximal value $f^* = 9$ is obtained, e.g., for $\xi = 0$. The shape of the distribution for $0 < f < 4$ is very close to that of the $T = 0$ distribution. The distribution for $4 < f < 9$ is due to higher excitons which are thermally populated at higher temperatures. A typical value of a higher exciton oscillator strength is $f = 8$, which is close to the maximal value $f = 9$ obtained for $\xi = 0$. This means that a potential well which traps the lowest exciton does not substantially affect the shape of the next exciton. Since for $\xi = 0$ there are two degenerate excitons with $f = 9$, one should expect in disordered aggregates the existence of another exciton with a large oscillator strength and with an energy close to that of the second exciton. This argument is supported by the distribution of f for $T = 100$ K presented in the lower panel of Figure 4b. In addition to the two features of the $T = 50$ K distribution whose shape does not change substantially, the $T = 100$ K distribution shows an additional peak at a very small value $f \approx 0.3$. This suggests that excitons populated at $T = 100$ K

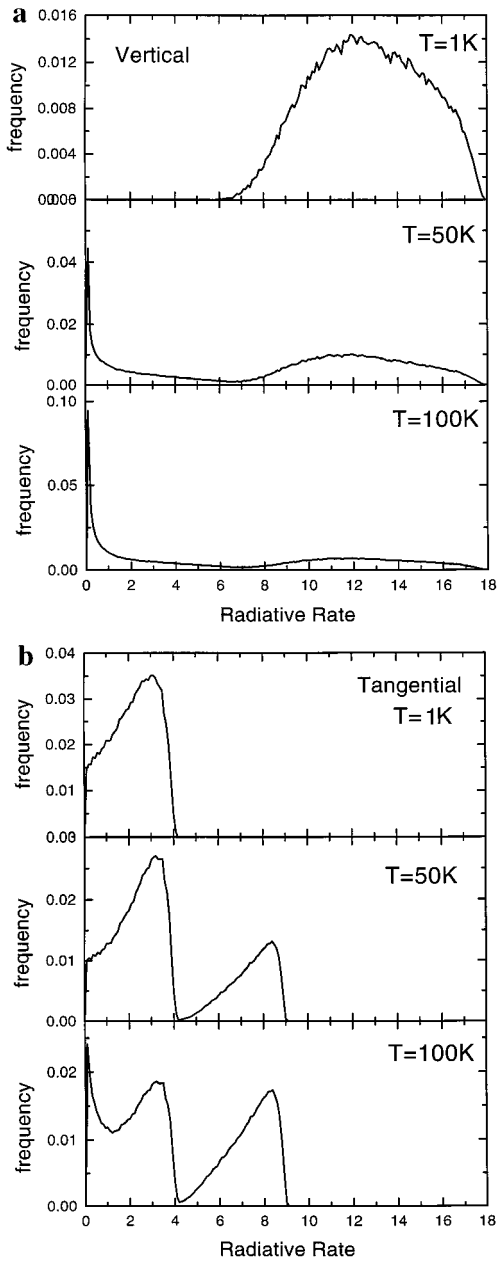

Figure 4. Distribution of excitonic radiative rates $P(f_\alpha)$ (in units of the single-molecule rate) for weak static disorder and various temperatures (as indicated in each panel). Calculations involved averaging over 100 000 realizations of static diagonal disorder with $\sigma = 190$ cm^{-1}. A bin size of 0.1 is used for the radiative rate to create the histogram: (a) vertical dipole configuration; (b) tangential dipole configuration.

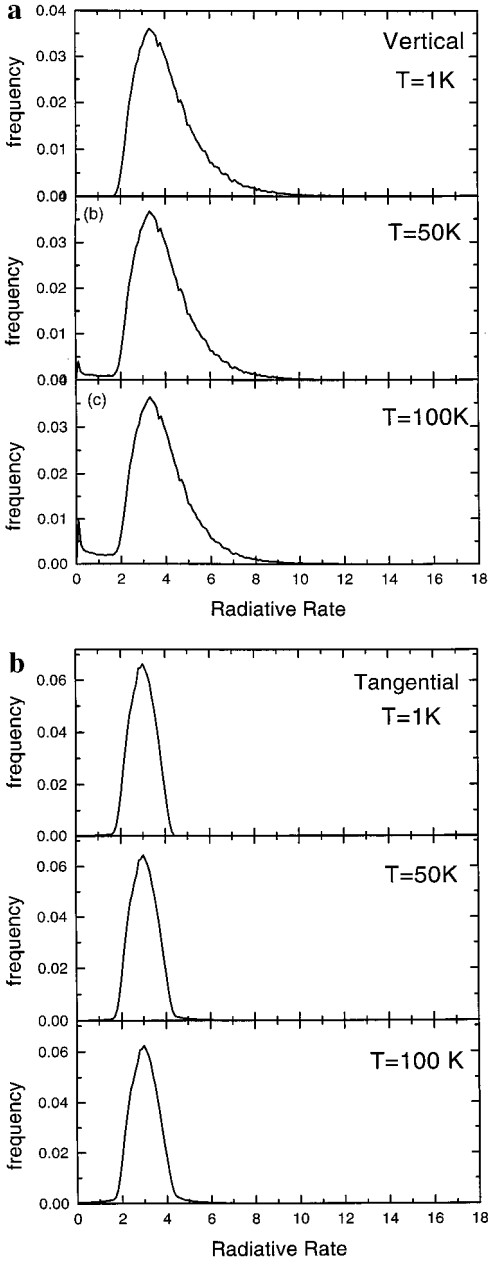

Figure 5. Same as in Figure 4 but for strong static disorder with $\sigma = 950$ cm^{-1}.

and not populated at $T = 50$ K carry very low oscillator strengths. Since the total oscillator strength is $N = 18$, and typical values are $f_0 = 3$ and $f_1 = 8$, there should be one additional exciton with $f_2 = 7$ to satisfy the sum rule. This picture is also confirmed by examining some particular realizations of disorder. A typical realization gives, e.g., $f_0 = 3$, $f_1 = 8$, and $f_2 = 6$, and the residual oscillator strength is distributed among the higher-energy excitons.

The distributions of individual exciton rates $P(f_\alpha)$ for strong disorder are presented in Figure 5. These distributions are similar to the corresponding distributions of Γ_S, indicating that only the lowest exciton is populated between 1 and 100 K.

IV. Polaronic Control of Superradiance

We now turn to a different mechanism for exciton localization, namely, dynamic localization due to exciton−phonon coupling and polaron formation. We follow the formalism of ref 16. Both diagonal and off-diagonal couplings were taken into account.[16,43]

Molecular aggregates generally interact with a bath consisting of nuclear (intramolecular, intermolecular, and solvent) degrees of freedom: Exciton−phonon interactions are described through the dependence of molecular frequencies Ω_n and intermolecular couplings J_{mn} on nuclear coordinates $\mathbf{q}$. We adopt the Holstein (molecular crystal) Hamiltonian:[44]

$$\hat{H} = \hat{H}^{\mathrm{ex}} + \hat{H}^{\mathrm{ph}} + \hat{H}^{\mathrm{ex-ph}} \tag{4.1}$$

$$\hat{H}^{\mathrm{ex}} = -J\sum_n B_n^\dagger (B_{n+1} + B_{n-1}) \tag{4.2}$$

$$\hat{H}^{\mathrm{ph}} = \hbar\omega_0 \sum_n b_n^\dagger b_n \tag{4.3}$$

$$\hat{H}^{\mathrm{ex-ph}} = g\hbar\omega_0 \sum_n B_n^\dagger B_n (b_n^\dagger + b_n) \tag{4.4}$$

Here $|0\rangle$ is the vacuum state for both the exciton and the phonon

degrees of freedom, and $B_n^\dagger$ ($b_n^\dagger$) creates an exciton (phonon) on site n. ω_0 is the Einstein phonon frequency, J is the exciton transfer integral between nearest-neighbor sites which will be measured in units of the Einstein frequency ω_0, and g is the diagonal exciton coupling strength. The Hamiltonian eq 4.1 can be obtained from eq 2.1 by expanding the molecular frequencies $\Omega_n(\mathbf{q})$ to first order in $\mathbf{q}$. We also assume nearest-neighbor intermolecular couplings J_{mn} and dispersionless (Einstein phonons).

We have computed the polaron wave function using the Toyazawa Ansatz:

$$|K\rangle = \sum_n e^{iKn} \sum_{n_1} \psi^K_{n_1-n} B^\dagger_{n_1} \exp[-\sum_{n_2} (\lambda^K_{n_2-n} b^\dagger_{n_2} - \lambda^{K*}_{n_2-n} b_{n_2})]|0\rangle \tag{4.5}$$

The parameters λ_n^K and ψ_n^K, as well as the energy of the lowest one-exciton band E^K, are obtained variationally.[48] In this Ansatz, the lattice phonon distortion λ_n^K and the exciton amplitude ψ_n^K share one common centroid. A localized polaron wave function from which a delocalizing procedure via the projection operator

$$\hat{P}(K) = N^{-1} \sum_n \exp[in(K - \sum_k k B_k^\dagger B_k - \sum_q q b_q^\dagger b_q)] \tag{4.6}$$

produces the Toyozawa Ansatz (4.5)

$$|K\rangle = \hat{P}(K)|D\rangle \tag{4.7}$$

where $|D\rangle$ is known as the Davydov solution in the context of vibrational energy transfer in protein:[45]

$$|D\rangle = \sum_n \psi_n(t) B_n^\dagger \exp[-\sum_n (\lambda_n(t) b_n^\dagger - \lambda_n^*(t) b_n)]|0\rangle \tag{4.8}$$

As pointed out by Čapek et al., extended states always yield lower variational energies than their parent localized states.[46] The Toyozawa Ansatz $|K\rangle$ is therefore a better trial wave function for the cyclic LH2 rings than the Davydov Ansatz $|D\rangle$.

The radiative decay rate (in units of the single chromophore rate) for the K'th polaron eigenstate $|K\rangle$ of the lowest one-exciton band is

$$\Gamma_K = |d_K|^2 = \sum_{mn} \mathbf{d}_m \cdot \mathbf{d}_n \langle K|K\rangle^{-1} \langle K|B_m^\dagger B_n|K\rangle \tag{4.9}$$

where we have taken into account the fact that $|K\rangle$ is not normalized. We have[16]

$$\langle K|B_m^\dagger B_n|K\rangle = \sum_{m'n'} e^{iK(n'-m')} \psi^{K*}_{m-m'} \psi^K_{n-n'} F^K_{n'm'} \tag{4.10}$$

where $F^K_{n'm'}$ is the Debye−Waller factor

$$F^K_{n'm'} = \exp[N^{-1} \sum_q |\lambda_q^K|^2 (e^{iq(m'-n')} - 1)] \tag{4.11}$$

with the Fourier-transformed phonon displacement λ_q^K defined as

$$\lambda_q^K = \sum_n e^{-iqn} \lambda_n^K \tag{4.12}$$

The characteristic length scale for $\langle K|B_m^\dagger B_n|K\rangle$ is determined by two factors, namely, the exciton amplitude ψ_n^K and the Debye−Waller factor $F^K_{n'm'}$ which represents the overlap of phonon wave functions.

TABLE 1: Polaron Energies and Radiative Rates for Vertical and Tangential Dipole Configurations and $J = 2\omega_0$[a]

K	E_K/ω_0	Γ_K vertical	Γ_K tangential	E_K/ω_0	Γ_K vertical	Γ_K tangential
0	−4.343	15.7	0.62	−5.541	8.46	1.93
$\pi/9$	−4.151	1.31	7.68	−5.463	2.60	4.59
$2\pi/9$	−3.715	3.95	1.90	−5.302	2.93	2.41
$\pi/3$	−3.431	8.81	2.45	−5.162	3.01	2.53
$4\pi/9$	−3.333	12.1	1.82	−5.066	3.90	2.50
$5\pi/9$	−3.298	13.8	1.33	−5.002	2.74	2.40
$2\pi/3$	−3.283	14.7	1.07	−4.962	2.61	2.31
$7\pi/9$	−3.278	15.3	0.87	−4.937	2.54	2.26
$8\pi/9$	−3.266	15.7	0.73	−4.923	2.50	2.23
π	−3.262	16.0	0.59	−4.919	2.48	2.22

[a] Two types of exciton−phonon couplings are considered. Left columns: weak coupling ($g = 1$). Right columns: medium coupling ($g = 2$). The average energy of the bare exciton band $-2J \cos K$ is set to zero.

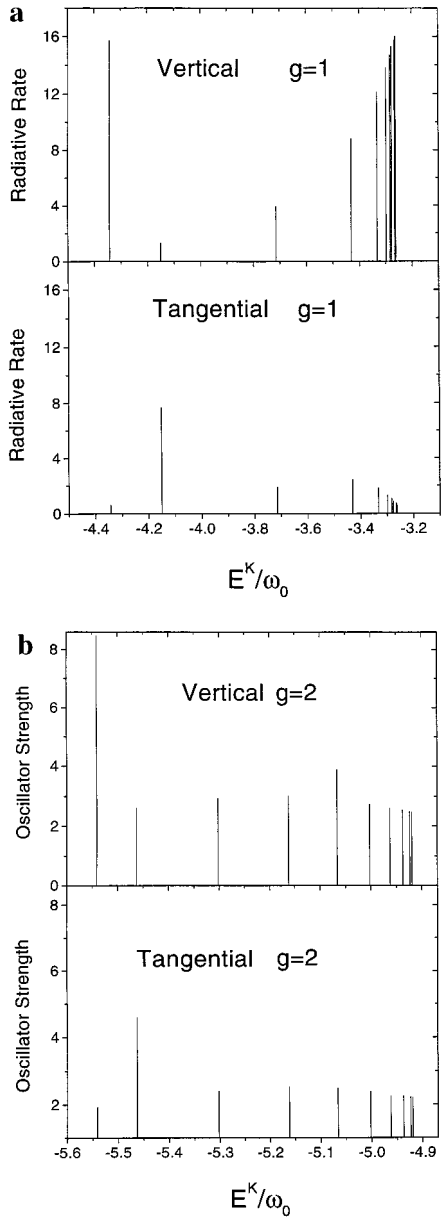

Figure 6. Radiative decay rates versus energy for polaron states (see Table 1): (a) $g = 1$, $J = 2\omega_0$; (b) $g = 2$, $J = 2\omega_0$.

The radiative rates and polaron energies for both dipole configurations (Figure 1) are listed in Table 1 for weak ($g = 1$, $J = 2\omega_0$) and medium ($g = 2$, $J = 2\omega_0$) exciton−phonon

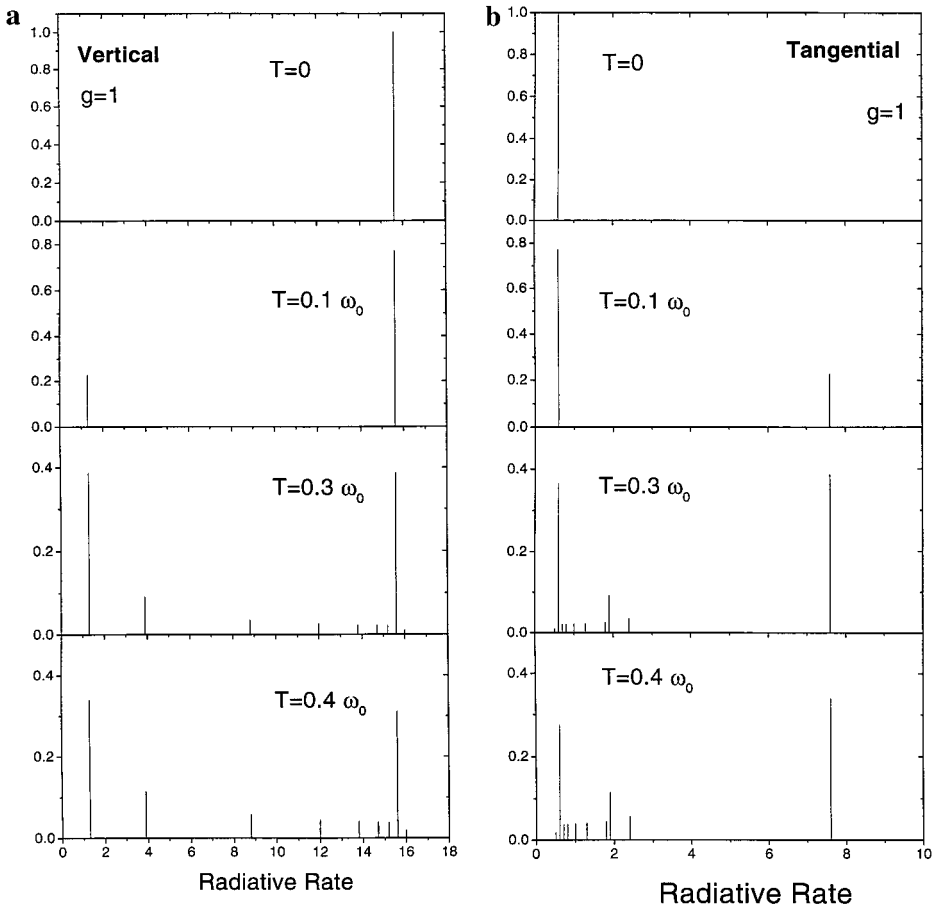

Figure 7. Distribution of radiative rates (in units of the single-molecule rate) for a weak-coupling polaron model ($g = 1$, $J = 2\omega_0$) and various temperatures (as indicated in each panel). A bin size of 0.1 is used for the radiative rate to create the histogram: (a) vertical dipole configuration; (b) tangential dipole configuration.

coupling. The average energy of the bare exciton band $-2J$ cos K is set to zero. The oscillator strengths of Table 1 are plotted versus the polaron energy in Figure 6. We have calculated the thermally averaged distribution of individual polaron rates $P(\Gamma_K)$. The contribution of the K'th state has been scaled by $Z^{-1} \exp(-E_K/k_BT)$ similar to the calculation of Figures 4 and 5. These distributions do not correspond to an experimental observation but merely provide an insight into the possible distributions of rates for slow exciton relaxation. In Figure 7a, we show the radiative rate distributions for the vertical model with weak exciton−phonon coupling. At zero temperature, only the $K = 0$ state is populated. As the temperature is increased, higher-energy eigenstates are populated and the distribution is shifted toward lower rates. As is clear from Table 1, the high-momentum states carry large oscillator strengths due to the fact that in these states phonons carry almost all of the crystal momentum leaving the exciton with zero momentum. Therefore the high momentum states are effectively excitons clothed by plane-wave phonons whose oscillator strengths resemble those of the $K = 0$ states at the bottom of the polaron band. Comparing Figure 7a with Figure 4a shows that in both cases, at low temperatures the distribution peaks at high radiative rates, whereas low-rate peaks emerge at high temperatures as the higher states are populated.

The situation is different for the tangential configuration, where only exciton momenta $k_{ex} = \pm\pi/9$ are selected, and the high-crystal-momentum states have vanishing oscillator strengths similar to the $K = 0$ state. This is demonstrated in Figure 7b where the low rate peak at 0.62 is attributed to $K = 0$ and the high rate peak at 7.68 represents the $K = \pm\pi/9$ states. Were the excitons not clothed by the phonon cloud, the $K = \pm\pi/9$ states would have an oscillator strength of 9. Phonon scattering introduced by eq 4.4 effectively reduces the exciton coherence. One can interpret Figure 7b qualitatively as Figure 7a with the x-axis reversed. The high-rate peaks in Figure 7a are then mapped onto the low-rate peaks in Figure 7b. The lowest peak in Figure 7a appears as the highest peak in Figure 7b, which corresponds to the $K = \pm\pi/9$ states. Temperature increase results in distributions between 0.59 and 2.45 which are attributed to states with higher crystal momenta. It is remarkable that the broad distribution from about 4 to 16 in Figure 7a is narrowed to the region below 3 in Figure 7b. This is analogous to Figure 4b where for low temperatures the distribution is confined between 0 and 4. However, the distribution from 4 to 8 in Figure 4b for higher temperatures does not appear in our polaron picture.

As the exciton−phonon coupling strength is increased to $g = 2$, the polaron bandwidth is reduced to about one-half the phonon frequency, implying that the gap below the phonon continuum is roughly the same as the bandwidth. Consequently, the oscillator strength for the vertical geometry has a weak momentum dependence for nonzero momentum eigenstates. Temperature increase lowers the probability of the radiative rate at which the $K = 0$ state emits, as more excitons are populated toward the higher lying states. In the low-rate regime the distribution is similar to strong static disorder (Figure 5a). In fact, the distribution peaks at about 3 in Figure 8, which is also comparable to Figure 5. (All peaks are between 2 and 3.) However, the $K = 0$ peak at 8.46 is absent in Figure 5a. Data for four different temperatures are shown. A bin size of 0.1

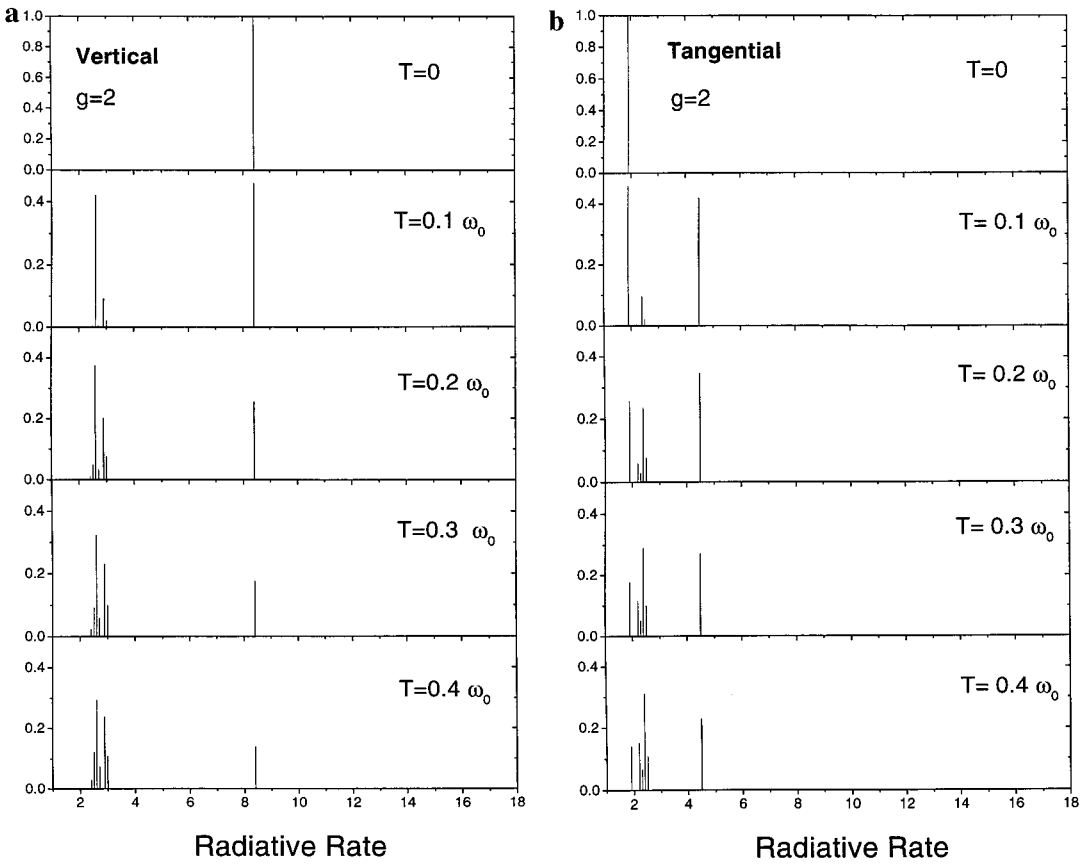

Figure 8. Same as in Figure 7 but for a medium-coupling polaron model ($g = 2$, $J = 2\omega_0$).

is used for the radiative rate to create the histogram. Therefore only six peaks are observed in Figure 8a instead of eight (excluding the $K = 0$ state). The distributions for the tangential dipole configuration are shown in Figure 8b. The peak at 4.6 is due to the $K = \pm 1/9\pi$ which exchanges position with the $K = 0$ peak in Figure 8a. The rest of the distribution is centered at about 3 as in Figure 8a. For $J = 2\omega_0$, the polaron self-trapping transition occurs at $g_c \approx 2.3$, where the effective mass of the phonon-dressed exciton is increased to more than 10 times the bare exciton mass.[43,47] The exciton amplitude ψ_n (but not the electronic excitation itself) is localized completely on a single site, and the superradiance factor is reduced to 1.[16] Although the exciton is still mobile in a strict, sense (delocalized wave function), the polaron bandwidth is so reduced that for all practical purposes the exciton is trapped in the lattice well it created. The distribution of radiative rates in this strong-coupling limit will be narrowly peaked at ~ 1.

The photophysics of antenna complexes is dominated by disorder. However, polaron effects are important for other types of aggregates. Radiative lifetimes of confined excitations in σ-conjugated systems such as polysilanes (linear chains) have been measured, and polaron models were used for their interpretation.[22] The 9- and 23-atom chains of polysilanes are found to correspond to the Toyozawa self-trapped and free states.[48] Exciton−phonon coupling is more pronounced in J aggregates of PIC which have an elongated two-dimensional structure.[49,50] Two-dimensional exciton delocalization is also found in J aggregates, of Langmuir−Blodgett films.[51]

V. Discussion

In this paper we have computed the distributions of radiative decay rates in circular aggregates for two extreme dipole orientations of chromophores. Applications have been made to the B850 band of the LH2 complex of the purple bacteria. Electronic excitations in light-harvesting complexes have recently been computed using the INDO-/S-CI code.[52] The results provide detailed descriptions of electronic state properties. The lower-energy excitations are found to be exciton type with delocalization over the entire aggregate. Starting with the Frenkel exciton model (eq 2.1), we have studied effects of static disorder and vibronic coupling on the radiative rate distributions. The absorption linewidth as well as the radiative rate formation in the LH2 complexes are dominated by the inhomogeneous (static disorder) mechanism.[4−8,15]

For the tangential configuration the same radiative rate $\Gamma_S \ll N$ can be obtained either when the off-diagonal size L_ρ of the one-exciton density matrix satisfies $L_\rho \ll N$ which yields $\Gamma_S \approx L_\rho$ or when $N - L_\rho \ll N$ and $\Gamma_S\ N - L_\rho$.[15,16] The two values of diagonal disorder used here yield about the same average value of Γ_S. For the weaker disorder ($\sigma = 190$ cm^{-1}) we have $\Gamma_S \approx N - L_\rho$, whereas for strong disorder ($\sigma = 950$ cm^{-1}) we have $\Gamma_S \approx L_\rho$. However, we have demonstrated that the distributions $P(\Gamma_S)$ are very different in the two cases. For weak disorder at $T = 1$ K the distribution $P(\Gamma_S)$ which reflects the distribution of the lowest exciton oscillator strength is broad, covers the range from $\Gamma_S = 0$ to $\Gamma_S^{(m)} = N/4 = 4.5$, and reaches its maximum at $\Gamma_S^* \approx 3$. At higher temperatures ($T = 50$ and 100 K) the distribution narrows with width $\Delta\Gamma_S \sim 0.5$ and is peaked at $\Gamma_S^* \approx 3.8$ and 4.2, respectively. We have proposed a compensating mechanism that predicts a substantial narrowing of the distribution with increasing temperature. The corresponding distributions for strong disorder are almost temperature-independent between $T = 1$ K and 100 K. Between $T = 50$ and 100 K, the strong disorder distribution which represents basically the lowest exciton oscillator strength is much broader than that for weak disorder.

The striking difference in the temperature dependence of the distribution for weak and strong disorder implies that one can distinguish between the two, either by SMS or by examining the temperature dependence of the time-resolved fluorescence signal $S(\tau)$.

The distribution $P(\Gamma_S)$ is important for interpreting energy transfer between antenna complexes. For example, for $\sigma = 190\ \mathrm{cm}^{-1}$ (which applies to the LH2 systems) the aggregate with more localized lowest exciton states have larger radiative rates as well as lower energies of the lowest exciton. Since at low temperatures energy transfer is biased toward lower energies, the correlation between the lowest exciton energy and the radiative rate leads to the depopulation of the low-energy states which makes the low-temperature energy transfer faster.

Acknowledgment. We wish to thank Dr. Oscar Somsen for useful discussions. The support of the National Science Foundation through Grants PHY94-15583 and CHE-9526125 and the Air Force Office of Scientific Research through Grant AFOSR-95-F49620-96-1-0030 is gratefully acknowledged.

References and Notes

(1) McDermott, G.; Prince, S. M.; Freer, A. A.; Hawthornthwaite-Lawless, A. M.; Papiz, M. Z.; Cogdell, R. J.; Isaacs, N. W. *Nature* **1995**, *374*, 517. Freer, A. A.; Prince, S. M.; Sauer, K.; Papiz, M. Z.; Hawthornthwaite-Lawless, A. M.; McDermott, G.; Cogdell, R. J.; Isaacs, N. W. *Structure* **1996**, *4* 449.

(2) Bradforth, S. E.; Jimenez, R.; von Mourik, F.; van Grondelle, R.; Fleming, G. R. *J. Phys. Chem.* **1995**, *99*, 16179.

(3) Jimenez, R.; Dikshit, S. R.; Bradforth, S. E.; Fleming, G. R. *J. Phys. Chem.* **1996**, *100*, 6825.

(4) van der Laan, H.; Schmidt, Th.; Visschers, R. W.; Visscher, K. J.; van Grondelle, R.; Völker, S. *Chem. Phys. Lett.* **1990**, *170*, 231.

(5) Reddy, N. R. S.; Small, G. J.; Seibert, M.; Picorel, P. *Chem. Phys. Lett.* **1991**, *181*, 391.

(6) Reddy, N. R. S.; Cogdell, R. J.; Zhao, L.; Small, G. J. *Photochem. Photobiol.* **1993**, *57*, 35.

(7) De Caro, C.; Visschers, R. W.; van Grondelle,. R.; Völker, S. *J. Phys. Chem.* **1994**, *98*, 10584.

(8) Wu, H.-M.; Rätsep, M.; Jankowiak, R.; Cogdell, R. J.; Small, G. J. *J. Phys. Chem. B* **1998**, *102*, 4023.

(9) Pullerits, T.; Chachisvilis, M.; Sundström, V. *J. Phys. Chem.* **1996**, *100*, 10787.

(10) Pullerits, T.; Chachisvilis, M.; Jones, M. R.; Hunter, C. N.; Sundström, V. *Chem. Phys. Lett.* **1994**, *224*, 355.

(11) Nagarajan, V.; Alden, R. G.; Williams, J. C.; Parson, W. W. *Proc. Natl. Acad. Sci. U.S.A.* **1996**, *93*, 13774.

(12) Leupold, D.; Stiel, H.; Teuchner, K.; Nowak, F.; Sander, W.; Ücker, B.; Scheer, H. *Phys. Rev. Lett.* **1996**, *77*, 4675.

(13) Joo, T.; Jia, Y.; Yu, J.-Y; Jonas, D. M.; Fleming, G. R. *J. Phys. Chem.* **1996**, *100*, 2399.

(14) Jimenez, R.; van Mourik, F.; Fleming, G. R. *J. Phys. Chem. B* **1997**, *101*, 7350.

(15) Meier, T.; Chernyak, V.; Mukamel, S. *J. Phys. Chem. B* **1997**, *37*, 7332.

(16) Meier, T.; Zhao, Y.; Chernyak, V.; Mukamel, S. *J. Chem. Phys.* **1997**, *107*, 3876.

(17) Feldmann, J.; Peter, G.; Göbel, E. O.; Dawson, P.; Moore, K.; Foxon, C.; Elliott, R. *J. Phys. Rev. Lett.* **1987**, *59*, 2337.

(18) Hübner, M.; Kuhl, J.; Stroucken, T.; Knorr, A.; Koch, S. W.; Hey, R.; Ploog, K. *Phys. Rev. Lett.* **1996**, *76*, 4199. Stroucken, T.; Knorr, A.; Thomas, P.; Koch, S. W. *Phys. Rev. B* **1996**, *53*, 2026.

(19) Brandes, T.; Inoue, J.; Shimizu, A. *Phys. Rev. Lett.* **1998**, *80*, 3952.

(20) Agranovich, V. M.; Basko, D. M.; Dubovsky, O. A. *J. Chem. Phys.* **1997**, *106*, 3896.

(21) Oberli, D. Y.; Vouilloz, F.; Kapon, E. *Phys. Status Solidi A* **1997**, *164*, 353.

(22) Thorne, J. R. G.; Williams, S. A.; Hochstrasser, R. M.; Fagan, P. J. *Chem. Phys.* **1991**, *157*, 401.

(23) Fleury, L.; Zumbusch, A.; Orrit, M.; Brown, R.; Bernard, R. *J. Lumin.* **1993**, *56*, 15.

(24) Monshouwer, R.; Abrahamsson, M.; van Mourik, F.; van Grondelle, R. *J. Phys. Chem. B* **1997**, *101*, 7241.

(25) Bopp, M. A.; Jia, Y.; Li, L.; Cogdell, R. J.; Hochstrasser, R. M. *Proc. Natl. Acad. Sci. U.S.A.* **1997**, *94*, 10630.

(26) Moerner, W. E.; Kador, L. *Phys. Rev. Lett.* **1989**, *65*, 2535.

(27) Basché, Th.; Ambrose, W. P.; Werner, W. E. *J. Opt. Soc. Am.* **1992**, *B9*, 829.

(28) Moerner, W. E. *Science* **1994**, *265*, 46. Moerner, W. E. and Orrit, M. *Science* **1999**, *283*, 1670.

(29) Orrit, M.; Bernard, J. *Phys. Rev. Lett.* **1990**, *65*, 2716.

(30) Basché, Th.; Moerner, W. E. *Nature* **1992**, *355*, 335.

(31) Basché, T.; Moerner, W.; Orrit, M.; Wild, E. U. P. *Single-Molecule Optical Detection, Imaging and Spectroscopy*; VCH: Weinheim, 1996.

(32) Orrit, M.; Bernard, J.; Zumbusch, A.; Personov, R. I. *Chem. Phys. Lett.* **1992**, *196*, 595; **1992**, *199*, 408.

(33) Lu, H. P.; Xie, X. S. *Nature* **1997**, *385*, 143. Xie, X. S. *Ace. Chem. Res.* **1996**, *29*, 598. Bian, R. X.; Dunn, R. C.; Xie, X. S.; Leung, P. T. *Phys. Rev. Lett.* **1995**, *75*, 4772.

(34) Trautman, J. K.; Macklini, J. J.; Brus, L. E.; Betzig, E. *Nature (London)* **1994**, *369*, 40.

(35) Macklini, J. J.; Trautman, J. K.; Harris, T. D.; Brus, L. E. *Science* **1996**, *272*, 255.

(36) Bopp, M. A.; Jia, Y.; Haran, G.; Morlina, E. A.; Hochstrasser, R. M. *Appl. Phys. Lett.* **1998**, *73*, 7.

(37) Plakhotnik, T.; Walser, D. *Phys. Rev. Lett.* **1998**, *80*, 4064.

(38) van Oijen, A. M.; Ketelaars, M.; Köhler, J.; Aartsma, T. J.; Schmidt, J. *J. Phys. Chem. B* **1998**, *102*, 9363.

(39) Sauer, K.; Cogdell, R. J.; Prince, S. M.; Freer, A. A.; Isaacs, N. W.; Scheer, H. *Photochem. Photobioi.* **1996**, *64*, 564.

(40) *J-Aggregates*; Kobayashi, T., Ed.; World Scientific: Singapore, 1996.

(41) Chernyak, V.; Meier, T.; Tsiper, E. V.; Mukamel, S. To be published.

(42) Chernyak, V.; Meier, T.; Mukamel, S. To be published.

(43) Zhao, Y. Ph.D. Thesis, University of California, San Diego, 1994. Zhao, Y.; Brown, D. W.; Lindenberg, K. *J. Chem. Phys.* **1997**, *107*, 3159; 3179 **1997**, *106*, 2728, 5622; **1994**, *100*, 2335.

(44) Holstein, T. *Ann. Phys. N.Y.* **1959**, *8*, 325, 343.

(45) Davydov, A. S. *Phys. Status Solidi* **1969**, *36*, 211. Davydov, A. S.; Kislukha, *N.* I. *Phys. Status Solidi* **1973**, *59*, 465. Davydov, A. S. *J. Theoret. Biol.* **1973**, *38*, 559.

(46) Capek, V.; Krausová, D. *Czech. J. Phys. B* **1987**, *37*, 1201.

(47) Lindenberg, K.; Zhao, Y.; Brown, D. W. In *Computational Physics*; Garrido, P., Marro, J., Eds.; Springer: Berlin, 1997; p 3.

(48) Toyozawa, Y. *J. Lumin.* **1976**, *12−13*, 13.

(49) Higgins, D. A.; Reid, P. J.; Barbara, P. F. *J. Phys. Chem.* **1996**, *100*, 1174.

(50) Potma, E. O.; Wiersma, D. A. *J. Chem. Phys.* **1997**, *108*, 4894.

(51) Furuki, M.; Pu, L. S.; Sasaki, F.; Kobayashi, S.; Tani, T. *Appl. Phys. Lett.* **1998**, *72*, 2648.

(52) Cory, M. G.; Zerner, M. C.; Hu, X.; Schulten, K. *J. Phys. Chem. B* **1998**, *102*, 7640.